

UvA-DARE (Digital Academic Repository)

The opposing effects of isotropic and anisotropic attraction on association kinetics of proteins and colloids

Newton, A.C.; Kools, R.; Swenson, D.W.H.; Bolhuis, P.G.

DOI

[10.1063/1.5006485](https://doi.org/10.1063/1.5006485)

Publication date

2017

Document Version

Final published version

Published in

Journal of Chemical Physics

License

Article 25fa Dutch Copyright Act (<https://www.openaccess.nl/en/policies/open-access-in-dutch-copyright-law-taverne-amendment>)

[Link to publication](#)

Citation for published version (APA):

Newton, A. C., Kools, R., Swenson, D. W. H., & Bolhuis, P. G. (2017). The opposing effects of isotropic and anisotropic attraction on association kinetics of proteins and colloids. *Journal of Chemical Physics*, 147(15), Article 155101. <https://doi.org/10.1063/1.5006485>

General rights

It is not permitted to download or to forward/distribute the text or part of it without the consent of the author(s) and/or copyright holder(s), other than for strictly personal, individual use, unless the work is under an open content license (like Creative Commons).

Disclaimer/Complaints regulations

If you believe that digital publication of certain material infringes any of your rights or (privacy) interests, please let the Library know, stating your reasons. In case of a legitimate complaint, the Library will make the material inaccessible and/or remove it from the website. Please Ask the Library: <https://uba.uva.nl/en/contact>, or a letter to: Library of the University of Amsterdam, Secretariat, P.O. Box 19185, 1000 GD Amsterdam, The Netherlands. You will be contacted as soon as possible.

UvA-DARE is a service provided by the library of the University of Amsterdam (<https://dare.uva.nl>)

The opposing effects of isotropic and anisotropic attraction on association kinetics of proteins and colloids

Arthur C. Newton, Ramses Kools, David W. H. Swenson, and Peter G. Bolhuis
*Van 't Hoff Institute for Molecular Sciences, Universiteit van Amsterdam, Science Park 904,
1098 XH Amsterdam, The Netherlands*

(Received 17 May 2017; accepted 22 September 2017; published online 16 October 2017)

The association and dissociation of particles via specific anisotropic interactions is a fundamental process, both in biology (proteins) and in soft matter (colloidal patchy particles). The presence of alternative binding sites can lead to multiple productive states and also to non-productive “decoy” or intermediate states. Besides anisotropic interactions, particles can experience non-specific isotropic interactions. We employ single replica transition interface sampling to investigate how adding a non-productive binding site or a nonspecific isotropic interaction alters the dimerization kinetics of a generic patchy particle model. The addition of a decoy binding site reduces the association rate constant, independent of the site’s position, while adding an isotropic interaction increases it due to an increased rebinding probability. Surprisingly, the association kinetics becomes non-monotonic for a tetramer complex formed by multivalent patchy particles. While seemingly identical to two-particle binding with a decoy state, the cooperativity of binding multiple particles leads to a kinetic optimum. Our results are relevant for the understanding and modeling of biochemical networks and self-assembly processes. *Published by AIP Publishing.* <https://doi.org/10.1063/1.5006485>

I. INTRODUCTION

Association and dissociation of proteins, such as proteins binding to DNA,¹ ligands binding to receptors, and proteins forming multicomponent complexes, are basic steps in many biochemically relevant processes such as gene regulation, signaling, and intercellular communication.^{2–7} Knowledge of the association and dissociation kinetics is crucial for understanding the balance of the biochemical network and cascade reactions and why such reactions are of processive or distributive nature.^{8,9} Proteins usually bind via specific interaction sites in a diffusion-influenced reaction to form a productive target structure,^{3,10} stabilized by specific hydrophobic interaction, hydrogen bonds, or electrostatic interactions, which can be modeled by *anisotropic*, angular dependent potentials^{11,12} (provided large conformational changes do not play a role). Proteins and protein complexes can have several similar or identical target sites, leading to multiple productive bound states.^{8,13} Interactions can also lead to a trapped *decoy* state: a (metastable) on- or off-pathway intermediate state. Finally, proteins interact with an (more or less) isotropic effective potential, for instance, due to van der Waals or depletion forces.^{6,14} Because of the anisotropic effective interaction, the possibility of multiple (rebinding) pathways, and the presence of isotropic potentials, it is not trivial to predict how additional non-specific sites affect the overall association rate constant towards a productive target structure.

Anisotropic interactions also play a role in the design of novel self-assembled materials, as colloidal particles with specific binding sites can be synthesized.^{15,16} The particles’ patchiness and multi-valency alter the kinetic pathways they take to reach the most stable state and subsequently form

higher order phases.^{11,17–19} Detailed knowledge of association kinetics helps us to understand and design complex colloidal self-assembly.²⁰

The major question that we address here is as follows: How does the association kinetics depend on the location, strength, and shape (anisotropic or isotropic) of additional non-productive interactions? To answer this fundamental question we employ molecular simulation of a general patchy-particle model that can represent proteins and patchy colloids.^{12,21–26} Neglecting hydrodynamics, simulating proteins, or colloids dynamics in a solution requires a stochastic technique such as Brownian dynamics or Dynamic Monte Carlo (DMC).²⁷ As brute force calculation of accurate (un)binding rate constants is hampered by large energetic and entropic barriers caused by strong binding and anisotropy of the interaction, we employ the Single Replica Transition Interface Sampling (SRTIS) method,^{28,29} an advanced path sampling method enabling numerically the exact treatment of the association and dissociation kinetics by efficient generation of unbiased rare pathways of all the relevant transitions. The combination of the simplified protein model and SRTIS gives us the ability to study many interaction parameters, which would otherwise be intractable, but we stress that our results generalize to arbitrarily complex potentials.

In the first part of this work, we focus on dimerization kinetics, where we find that anisotropic decoy interactions act as kinetic traps and suppress association kinetics but that an additional isotropic interaction opposes this effect and enhances association kinetics again. We show, using our path sampling methodology, how this kinetic enhancement is largely due to rebinding pathways to the target state. Having thus set the stage, in the second part, we investigate

association kinetics of a larger cluster, in this case a tetramer. Surprisingly, as a function of the isotropic interaction strength, the tetramer association kinetics behaves non-monotonically. An initial enhancement in association is offset by a complete suppression at a higher isotropic strength. Using the insights obtained from the dimerization kinetics, we can explain these opposing effects in terms of an induced decoy state due to cooperative interactions.

The remainder of the paper is organized as follows. After a description of the used model, the DMC dynamics, and the SRTIS method, we present and discuss the results. We end with concluding remarks.

II. METHODS

A. Model

For the case of two-particle dimerization, we consider two particles where one particle (1) has two binding sites, one target t , and one decoy site d , whereas the other particle (2) has only one binding site b (see Fig. 1). This system has three metastable states: a bound (target) state T when site b is bound to target site t , a nonproductive decoy state D when site b is bound to decoy site d , and an unbound state U when particles are far apart. We model the interaction between the particles and the patches based on a 24-12 Lennard-Jones (LJ)-like potential. This potential is of shorter range than the standard 12-6 Lennard-Jones (LJ) potential. As such the phase behavior of a many-particle system exhibits a metastable liquid vapor coexistence line with respect to the gas solid coexistence,³⁰ similar to protein solutions.

The total potential is a superposition of a strongly repulsive Weeks-Chandler-Andersen-like potential,^{31,32} an isotropic attractive potential, and the minimum of two attractive anisotropic angle dependent potentials,

$$U_{12}(\mathbf{r}_{12}, \Omega_1, \Omega_2) = U_{rep}(\mathbf{r}_{12}) + U_{iso}(\mathbf{r}_{12}) + \min [U_{bt}(\mathbf{r}_{12}, \Omega_1, \Omega_2), U_{bd}(\mathbf{r}_{12}, \Omega_1, \Omega_2)], \quad (1)$$

where $\mathbf{r}_{12} = \mathbf{r}_2 - \mathbf{r}_1$ is the inter-particle vector with \mathbf{r}_i the coordinates of particle i and $\Omega_{1,2}$ denote the orientations of the particles, stored in quaternion form. The min function returns

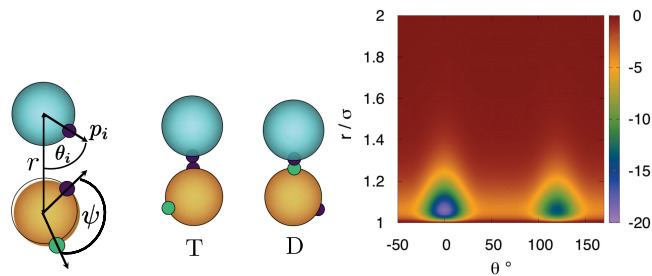


FIG. 1. Left: Cartoon image of the patchy particle model (particle 1 orange, particle 2 blue) with the angle between decoy and target site, ψ , distance between particles $r = |\mathbf{r}_{12}|$, patch (unit) vector \mathbf{p}_i , and corresponding angle θ_i . Middle: states T and D are depicted. Right: Potential energy surface as a function of the distance between particles, r , and the shift in orientation, θ for $\psi = 120^\circ$, $\epsilon_D = 10k_B T$, $\epsilon_T = 15k_B T$, $\epsilon_{iso} = 4k_B T$, $\delta = 20^\circ$ showing clearly the two potential minima due to the two patches and additionally the low isotropic attraction.

the smaller of its arguments and is introduced to avoid spurious interference of two patchy interactions that are near each other. The isotropic WCA-like repulsive potential is given by

$$U_{rep}(\mathbf{r}_{12}) = \begin{cases} 4.0 \left[\left(\frac{\sigma}{r} \right)^{24} - \left(\frac{\sigma}{r} \right)^{12} + \frac{1}{4} \right] & \text{if } r \leq 2^{\frac{1}{12}} \sigma \\ 0 & \text{if } r > 2^{\frac{1}{12}} \sigma \end{cases}, \quad (2)$$

where $r = |\mathbf{r}_{12}|$ is the distance between particles and σ determines the diameter of the particle. This repulsive interaction provides the basic hard core interaction, even in the absence of the isotropic potential. The isotropic interaction is given by

$$U_{iso}(\mathbf{r}_{12}) = \begin{cases} 4.0 \epsilon_{iso} \left[\left(\frac{\sigma}{r} \right)^{24} - \left(\frac{\sigma}{r} \right)^{12} \right] & \text{if } r \leq r_c \\ 0 & \text{if } r > r_c \end{cases}, \quad (3)$$

where ϵ_{iso} is the strength of the isotropic potential and r_c is the potential cutoff, beyond which the potential vanishes. For simplicity, we took a Lennard-Jones-like form. The repulsive part of this isotropic potential will also contribute to the hard core nature of the particle. The anisotropic patchy interaction between b and t is given for $r \leq r_c$ by

$$U_{bt}(\mathbf{r}_{12}, \Omega_1, \Omega_2) = 4.0 \epsilon_T \left[\left(\frac{\sigma}{r} \right)^{24} - \left(\frac{\sigma}{r} \right)^{12} \right] \mathcal{S}_{bt}(\mathbf{r}_{12}, \Omega_1, \Omega_2) \quad (4)$$

and zero otherwise, where ϵ_T is the strength of the patchy interaction between b and t . The patchy interaction between b and d is defined similarly,

$$U_{bd}(\mathbf{r}_{12}, \Omega_1, \Omega_2) = 4.0 \epsilon_D \left[\left(\frac{\sigma}{r} \right)^{24} - \left(\frac{\sigma}{r} \right)^{12} \right] \mathcal{S}_{bd}(\mathbf{r}_{12}, \Omega_1, \Omega_2), \quad (5)$$

where ϵ_D is the strength of the patchy interaction between b and d . The continuous patch function $\mathcal{S}_{ij}(\Omega_1, \Omega_2)$ gives a penalty for misalignment,

$$\mathcal{S}_{ij}(\mathbf{r}_{12}, \Omega_1, \Omega_2) = \exp\left(-\frac{\theta_i^2 + \theta_j^2}{2\delta^2}\right), \quad (6)$$

where δ defines the patch angular width, $\theta_i = \arccos(\mathbf{p}_i \cdot \mathbf{r}_{12}/r)$, $\theta_d = \arccos(\mathbf{p}_d \cdot \mathbf{r}_{12}/r)$, $\theta_b = \arccos(\mathbf{p}_b \cdot \mathbf{r}_{21}/r)$, with \mathbf{p}_k the (unit) vector defining patch p_k (with $k \in \{b, d, t\}$) on its respective particle (1 or 2), rotated from the particle frame to the system frame along $\Omega_{1,2}$. Note that for binding site b , the inter-particle vector $\mathbf{r}_{21} = -\mathbf{r}_{12}$ is reversed. Finally, we use the angle $\psi = \arccos(\mathbf{p}_d \cdot \mathbf{p}_t)$ to describe the angular distance between the patches d and t . The interaction between particles can be easily tuned via the patch-patch interaction strengths ϵ_T , ϵ_D , the isotropic interaction strength ϵ_{iso} , and the angular width δ . Proteins usually have a specific (narrow) patchy interaction; therefore, the patch-width is chosen to be small, $\delta = 20^\circ$. This patch-width was shown to reproduce the gas-liquid curves of protein solutions such as γ -crystallin and lysozyme quite well,³³ albeit with more patches. A similar patch width was used to study protein crystallization.¹² Naturally, an even smaller patch-width is also allowed by the model; however, a much smaller patch-width also dramatically restricts the time step in the dynamics. An example of the potential for the dimer is shown in Fig. 1.

For the constrained tetramer, we employed the same model between each pair of particles of the complex as for the

two-particle system. Each particle has three patches aligned along the vertices of the perfectly formed tetramer. There is no additional decoy site defined. The total energy for the constrained tetramer is

$$U_{tot}^{tet}(\mathbf{r}^4, \Omega^4) = \sum_{i < j}^4 U_{rep}(\mathbf{r}_{ij}) + U_{iso}(\mathbf{r}_{ij}) + \sum_{i < j}^4 \sum_{k < l}^3 U_{kl}(\mathbf{r}_{ij}, \Omega_i, \Omega_j), \quad (7)$$

where the superscript 4 denotes the fact that all particle positions \mathbf{r} and orientations Ω are in principle taken into account. The first (double) sum on the r.h.s. is over each particle pair in the tetramer, and the second (double) sum is over the patch pairs k, l . The potential U_{kl} is defined similarly to Eq. (4).

B. Dynamic Monte Carlo

We use Dynamic Monte Carlo (DMC) to propagate the system in time. By using small translation and rotational step sizes, time evolution via MC dynamics numerically solves the Fokker-Planck equations which represent the Brownian movement of proteins in solution.^{21,27} A translation move displaces a randomly chosen particle by a random amount in the interval $[-\delta_t, \delta_t]$ and a rotation move rotates a randomly chosen particle over an angle randomly chosen between $[0, \delta_r]$. The maximum translational displacement is set to 0.005σ for all cases. The rotational step size is chosen to obey the rotational Stokes-Einstein relation, i.e.,

$$\frac{\delta_t}{\delta_r} = \sigma \sqrt{\frac{\bar{a}_r D_t}{\bar{a}_t 3D_r}}, \quad (8)$$

where D_t, D_r denote the translational and rotational diffusion constant, respectively, and the average translational and rotational acceptance ratios, \bar{a}_t and \bar{a}_r are always higher than 0.7. It has been demonstrated that this regime leads to proper diffusive dynamics.^{27,34}

Taking a colloidal suspension in water, with colloids of size $\sigma = 1 \mu\text{m}$, and using the Stokes-Einstein relation to compute the translational diffusion, $D_t^0 = k_B T / (3\pi\eta\sigma)$, we can estimate the actual time step as $\Delta t = \delta_r^2 \bar{a}_t / (6D_t^0)$. In the colloid case, every DMC cycle corresponds roughly to $7 \mu\text{s}$. For proteins, which are roughly a hundred times smaller, this time becomes $\sim 10^2$ ns.

C. Path sampling with SRTIS

Here we use Single Replica Transition Interface Sampling (SRTIS) to obtain the full (un)binding path ensemble between the defined stable states.^{28,29} A path is defined as $\mathbf{x}^L \equiv \{\mathbf{x}_0, \mathbf{x}_1, \dots, \mathbf{x}_L\}$, a series of L time frames or slices. Each frame is a point in configuration space $\mathbf{x} = \{\mathbf{r}^N, \Omega^N\}$, with \mathbf{r} and Ω the coordinates and orientation (in quaternion representation) of each particle in the N -particle system (note the difference between this definition and previous definitions in, e.g., Refs. 28, 29, 35, and 36, as here we do not carry the momenta, due to the use of DMC, but we do carry the orientation of the particles).

Consider a set of (meta)stable states \mathbf{M} . In the systems studied here, the states for the dimer are $\mathbf{M} \equiv \{T, D, U\}$ and

those for the tetramer are $\mathbf{M} \equiv \{U, T, I, D\}$. See Sec. III C for an explanation of these latter states. For each state $\mathcal{I} \in \mathbf{M}$, we define a set of m non-intersecting hypersurfaces (called interfaces³⁷) $\lambda_{\mathcal{I}} = \{\lambda_{\mathcal{I}}^0, \lambda_{\mathcal{I}}^1, \dots, \lambda_{\mathcal{I}}^m\}$ based on an order parameter λ (e.g., a distance or a potential energy). We use the convention here that for all interface and indicator functions, a superscript refers to the interface index, while a subscript denotes the state the interface belongs to. This notation is slightly different than in Refs. 28 and 29. Note that while each set of interfaces belonging to a state \mathcal{I} is non-intersecting, interfaces from different states are allowed to intersect. Also note that the first interface $\lambda_{\mathcal{I}}^0$ is located outside the definition of the stable state \mathcal{I} . See Sec. II G for precise stable state and interface definitions for the dimer and tetramer systems.

In SRTIS, a single replica performs a random walk among the interfaces while simultaneously sampling path space by employing five different path moves. The primary move is the one-way shooting move from a point at a current interface.³⁶ From the time slice at which the path first crosses the current interface, a partial trial path is generated either in the forward or backward direction and accepted if this partial path ends in any stable state, irrespective of the path length (there is of course a hard-coded maximum path length to prevent memory overflow). The complementary part of the full trajectory is taken from the old path.³⁶ Note that the acceptance ratio becomes close to unity because all generated paths already cross the interface. Due to the stochastic nature of the dynamics, the newly generated path will sample a different part of path space. In order to achieve decorrelation between pathways, the time-reversal move reverses the pathway in time, by reversing the order of the frames,³⁵ and an inversion of the momenta for each frame (this is not needed for Brownian dynamics or DMC). In addition, we use replica swap and state swap moves. A replica swap move attempts to change the current interface to a neighbouring interface, under the condition that the path still crosses this new interface. Uniform sampling of all interfaces of a state is achieved by a Wang-Landau (WL) algorithm, with the acceptance criterion for a replica swap between interfaces i and j ,

$$P_{acc}(\mathbf{x}^L; \lambda_{\mathcal{I}}^i \rightarrow \lambda_{\mathcal{I}}^j) = \tilde{h}_{\mathcal{I}}^j[\mathbf{x}^L] \min \left[1, \frac{g_{\mathcal{I}}(\lambda_{\mathcal{I}}^i)}{g_{\mathcal{I}}(\lambda_{\mathcal{I}}^j)} \right], \quad (9)$$

where the min function returns the smaller of its arguments and $\tilde{h}_{\mathcal{I}}^j[\mathbf{x}^L]$ is a trajectory indicator function that is unity only if the path starts in \mathcal{I} , crosses interface $\lambda_{\mathcal{I}}^j$, and ends in any stable state (including \mathcal{D}). The Wang-Landau bias is imposed through the density of paths $g_{\mathcal{I}}(\lambda_{\mathcal{I}}^j)$ which upon visiting $\lambda_{\mathcal{I}}^j$ is updated by multiplying with a Wang-Landau factor $\exp(f_{WL})$. At the start of the simulation, the densities of paths are initialized to $g(\lambda) = 1$ and $f_{WL} = 0.01$. Once all replicas have been sampled uniformly within a certain threshold, the WL factor is halved until sufficiently small ($f_{WL} < 10^{-5}$).²⁸

A state swap move attempts to change the current initial state to a different state when the path is of type $\mathcal{I} \rightarrow \mathcal{J}$ with $\mathcal{J} \neq \mathcal{I}$. This swap move requires a path-reversal, altering a path of type $\mathcal{I} \rightarrow \mathcal{J}$ into type $\mathcal{J} \rightarrow \mathcal{I}$. After the state swap, the set of interfaces belonging to the new initial state is used. The acceptance probability for the state swap is

$$P_{acc}(\mathbf{x}^L; \lambda_{\mathcal{I}}^i \rightarrow \lambda_{\mathcal{J}}^j) = \tilde{h}_{\mathcal{J}}^j[\overleftarrow{\mathbf{x}}^L] \min \left[1, \mathcal{R} \frac{g_{\mathcal{I}}(\lambda_{\mathcal{I}}^i)}{g_{\mathcal{I}}(\lambda_{\mathcal{J}}^j)} \right], \quad (10)$$

where the arrow to the left in $\overleftarrow{\mathbf{x}}^L$ denotes the reverse order of the trial path and the factor \mathcal{R} is unity if a state swap is performed only between the outermost interfaces or only between interfaces $\lambda_{\mathcal{I}}^k$ and $\lambda_{\mathcal{J}}^k$ with identical indices k , and $\mathcal{R} = m_{\mathcal{I}}/m_{\mathcal{J}}$ is the ratio of the number of replicas of states \mathcal{I} and \mathcal{J} if one allows swaps between all interfaces. When states are nested within interfaces, it can be advantageous to allow for all-interface state swaps.

Finally, to randomize within the stable states, we employ the so-called ‘‘minus move,’’^{36,38} sampling an additional first interface ensemble,³⁹ which lets the path evolve (backward or forward in time) within a state until it exits the state and crosses the first interface. The minus interface ensemble can always exchange with the first (regular) interface ensemble via replica exchange.

D. Rate constant calculation

The rate constant between any two states \mathcal{I} and \mathcal{J} is given by^{37,40}

$$k_{\mathcal{I}\mathcal{J}} = \Phi_{\mathcal{I}} P(\lambda_{\mathcal{J}}^0 | \lambda_{\mathcal{I}}^1), \quad (11)$$

where $\Phi_{\mathcal{I}}$ is the flux out of state \mathcal{I} through the innermost interface $\lambda_{\mathcal{I}}^1$ and $P(\lambda_{\mathcal{J}}^0 | \lambda_{\mathcal{I}}^1)$ is the conditional crossing probability to reach state \mathcal{J} from $\lambda_{\mathcal{I}}^1$, with $\lambda_{\mathcal{J}}^0$ the state definition of \mathcal{J} .

The flux is calculated as $\Phi_{\mathcal{I}} = (\langle \tau_{\mathcal{I}}^0 \rangle + \langle \tau_{\mathcal{I}}^1 \rangle)^{-1}$, where $\langle \tau_{\mathcal{I}}^0 \rangle$ is the average dwell time in the stable state \mathcal{I} , before crossing $\lambda_{\mathcal{I}}^1$, which can be calculated directly from the length of the pathways generated by the minus move. Correspondingly, $\langle \tau_{\mathcal{I}}^1 \rangle$ is the average time it takes from the first interface back to the stable state \mathcal{I} and follows directly from the length of the pathways sampled in the first interface replica.

It is interesting to note that the flux out of the unbound state U can change with the total simulation volume V . As for the unbound state, τ_U^0 is given by free diffusion when the particles are beyond 2.0σ apart, the dependence of τ_U^0 on volume V can be solved analytically, and the total flux out of state U is given by

$$\Phi_U = \left(\langle \tau_U^1 \rangle + \langle \tau_U^0 \rangle \frac{V}{V_0} \right)^{-1} \quad (12)$$

for arbitrary volume $V > V_0$, where V_0 denotes the volume at which the diffusive dwell time τ_U^0 is computed.

$P(\lambda_{\mathcal{J}}^0 | \lambda_{\mathcal{I}}^1)$ is calculated by joining all obtained crossing probabilities for every replica of a state via Weighted Histogram Analysis Method (WHAM).^{41,42} As we sample all association and dissociation transitions, we obtain the full rate $M \times M$ matrix \mathbf{K} (i.e., the matrix form of $k_{\mathcal{I}\mathcal{J}}$). Note that the obtained rate expressions are exact under the assumption of rare event (exponential) kinetics between the states. While the kinetics of diffusion-controlled association depends on dimensionality, in our work this kinetics is dominated by diffusion in three dimensions, for which the exploration of space is non-compact.⁴³ Even if the system can temporarily switch to a quasi-2D diffusion when particles are bound by an isotropic nonspecific potential, the corresponding time scales for this

diffusion in reduced dimensionality are (especially for larger volumes) always smaller than the time spent in the unbound state.

In a multiple state system, where states can be nested in between interfaces of other states, Eq. (11) is not valid anymore as it assumes that transitions can only occur when the outermost interface $\lambda_{\mathcal{I}}^m$ has been reached, which is not necessarily the case for systems which are nested in between interfaces of other states. If Eq. (11) is used naively, many transitions would be missed in the rate calculation. One can circumvent this problem by calculating the rate via the path-type numbers introduced in Ref. 29. A path-type number is defined as $n_{\mathcal{I}\mathcal{J}}^i(\lambda_{\mathcal{I}}^k)$, which in words is the number of paths in replica i joining states \mathcal{I} and \mathcal{J} that have crossed at maximum interface $\lambda_{\mathcal{I}}^k$ (and thus by definition also all interfaces below k). The superscript i indicates that the paths should obey the condition of replica i in the ensemble. Because we have set the maximum interface, we can reweight these numbers with the WHAM weights obtained from reweighting of the crossing probability as follows:

$$\bar{n}_{\mathcal{I}\mathcal{J}}(\lambda_{\mathcal{I}}^k) = \bar{w}_{\mathcal{I}}^k \sum_{i=1}^m n_{\mathcal{I}\mathcal{J}}^i(\lambda_{\mathcal{I}}^k), \quad (13)$$

with $\bar{w}_{\mathcal{I}}^k = (\sum_i^k 1/w_{\mathcal{I}}^i)^{-1}$, where $w_{\mathcal{I}}^i$ are the optimized WHAM weights for paths that have crossed interface $\lambda_{\mathcal{I}}^k$ at maximum (note that these should be the same as the weights $w_{\mathcal{I}}^i$ obtained via the crossing probability). Now we have the correctly reweighted number of paths $\bar{n}_{\mathcal{I}\mathcal{J}}(\lambda_{\mathcal{I}}^k)$ joining state \mathcal{I} with state \mathcal{J} that at maximum have crossed interface $\lambda_{\mathcal{I}}^k$. Subsequently summing over all interfaces k gives the reweighted number of paths coming from state \mathcal{I} and ending in state \mathcal{J} ,

$$\tilde{n}_{\mathcal{I}\mathcal{J}} = \sum_{k=1}^m \bar{n}_{\mathcal{I}\mathcal{J}}(\lambda_{\mathcal{I}}^k). \quad (14)$$

Because the Wang-Landau scheme biases the simulation to sample all states equally via the state-swap bias, the path-numbers for each state need to be corrected for this bias. In an unbiased ensemble, each $\mathcal{I}\mathcal{J}$ path is as likely as the reversed $\mathcal{J}\mathcal{I}$ path. Therefore, we split the obtained path-type matrix, $\bar{n}_{\mathcal{I}\mathcal{J}}$, into M matrices and symmetrize the \mathcal{I} th matrix: $\tilde{n}_{\mathcal{J}\mathcal{I}} = \bar{n}_{\mathcal{I}\mathcal{J}}$, setting all other entries of the \mathcal{I} th matrix to zero, resulting in M different matrices with only a nonzero \mathcal{I} th row and a nonzero \mathcal{J} th column. Subsequently, all M matrices are joined via WHAM giving the individual weights for each state [these weights can also be used to calculate the coefficients, $c_{\mathcal{I}}$, in the reweighted path probability, see Eq. (16)]. This leads to a $M \times M$ transition path type number matrix, $\tilde{n}_{\mathcal{I}\mathcal{J}}$. Normalizing the matrix with the total numbers of paths going out of a state $\sum_{\mathcal{J}} \tilde{n}_{\mathcal{I}\mathcal{J}}$ yields

$$P(\lambda_{\mathcal{J}}^0 | \lambda_{\mathcal{I}}^1) = \frac{\tilde{n}_{\mathcal{I}\mathcal{J}}}{\sum_{\mathcal{J} \in M} \tilde{n}_{\mathcal{I}\mathcal{J}}}. \quad (15)$$

This normalized transition probability matrix can be directly used in Eq. (11).

E. Free energy landscapes and Reactive Path Density (RPD) from the reweighted path ensemble

In SRTIS, we obtain the Wang-Landau biased path ensemble for each state $\mathcal{I} \in \mathbf{M}$. We can reweight this biased path

ensemble, by using the same WHAM reweighting procedure as explained above. Defining the phase space volume $\Lambda_{\mathcal{I}}^j = \{\mathbf{x} | \lambda(\mathbf{x}) > \lambda_{\mathcal{I}}^j\}$ as the volume outside interface $\lambda_{\mathcal{I}}^j$, the reweighted path probability $\mathcal{P}_{RPE}[\mathbf{x}^L]$ for observing a path \mathbf{x}^L in an unbiased path ensemble is

$$\mathcal{P}_{RPE}[\mathbf{x}^L] = \sum_{\mathcal{I} \in \mathbf{M}} c_{\mathcal{I}} \left[w_{\mathcal{I}}^1 P_{\Lambda_1}^-[\mathbf{x}^L] + \sum_{j=1}^{n-1} \mathcal{P}_{\Lambda_j}[\mathbf{x}^L] W_{\mathcal{I}}[\mathbf{x}^L] \right], \quad (16)$$

where \mathcal{P}_{Λ_j} and $P_{\Lambda_1}^-$ denote the (biased) path probability for interface j of state \mathcal{I} and the minus interface, respectively. (In Ref. 39, this minus interface ensemble is labeled as ‘‘additional first interface ensemble.’’) Note also that we rearranged the sub- and superscripts with respect to Refs. 28, 29, and 39 to be consistent with the discussion in Secs. II C and II D.) The constants $c_{\mathcal{I}}$ are obtained via matching the density of paths, $g_{\mathcal{I}}[\mathbf{x}^L]$, between states. The factor $W_{\mathcal{I}}[\mathbf{x}^L] = \sum_{i=1}^{n-1} \bar{w}_{\mathcal{I}}^i \theta(\lambda_{\mathcal{I}}^{\max}[\mathbf{x}^L] - \lambda_{\mathcal{I}}^i) \theta(\lambda_{i+1} - \lambda_{\mathcal{I}}^{\max}[\mathbf{x}^L])$ selects the correct weight $\bar{w}_{\mathcal{I}}^i$ for a path that has its maximum λ between interfaces i and $i + 1$. Here, $\theta(x)$ denotes the Heaviside theta function and $\lambda^{\max}[\mathbf{x}^L]$ returns the maximum λ value along a path. Similar to Sec. II D, $\bar{w}_{\mathcal{I}}^i = (\sum_{j=1}^i 1/w_{\mathcal{I}}^j)^{-1}$, where $w_{\mathcal{I}}^j$ are the optimized WHAM weights for each interface histogram. Note that this reweighting is on the full trajectories and not on the crossing histograms only.⁴⁴

From the reweighted path ensemble, we can calculate the free energy landscape $F(\mathbf{q})$,³⁹

$$F(\mathbf{q}) = -k_B T \log p(\mathbf{q}) + \text{const}, \quad (17)$$

$$p(\mathbf{q}) = C \int \mathcal{D}\mathbf{x}^L \mathcal{P}_{RPE}[\mathbf{x}^L] \sum_{k=0}^L \delta[\mathbf{q}(\mathbf{x}_k) - \mathbf{q}],$$

where $p(\mathbf{q})$ is the equilibrium probability to observe a (combination of) collective variable(s) \mathbf{q} , C is a normalizing constant, $\int \mathcal{D}\mathbf{x}^L$ is the (formal) path integral over the ensemble of pathways \mathbf{x}^L , $\mathbf{q}(\mathbf{x}_k)$ denote the collective variables (e.g., for the dimer and tetramer systems studied here, the angle ϕ and the distance r , see Sec. III) at time slice \mathbf{x}_k . The sum over delta functions projects each slice of the reweighted paths on the collective variable space \mathbf{q} to yield the probability $p(\mathbf{q})$.

The reactive path density is defined as³⁹

$$n_r(\mathbf{q}) = \int \mathcal{D}\mathbf{x}^L \mathcal{P}_{RPE}[\mathbf{x}^L] h_{\mathcal{I}}(\mathbf{x}_0) h_{\mathcal{J}}(\mathbf{x}_L) h_{\mathbf{q}}(\mathbf{x}^L), \quad (18)$$

where the function $h_{\mathbf{q}}(\mathbf{x}^L)$ is unity if the path visits \mathbf{q} , and zero otherwise. $h_{\mathcal{I}}(\mathbf{x}_0)$ and $h_{\mathcal{J}}(\mathbf{x}_L)$ ensure that only reactive pathways are taken into account. Note that a path density does not add up to unity.

F. Transition Path Theory (TPT)

In order to understand how non-specific binding affects the overall binding rate, the rate from U to D and D to T has to be considered (and the corresponding rates to I for the tetramer). Transition Path Theory (TPT) allows us to calculate the overall association rate k_{UT}^{TPT} .⁴⁵ An important quantity in this framework is the committor probability, q_i^+ , which for binding processes is the probability to reach the bound state, T , from intermediate state i before reaching the unbound state U . By definition, $q_U^+ = 0$ and $q_T^+ = 1$. Generally speaking, the

other committor probabilities are given by solving a linear set of equations,

$$q_i^+ = \sum_{k \in \mathbf{I}} T_{ik} q_k^+ + T_{iT}, \quad (19)$$

where $\mathbf{T} = \exp(\mathbf{K}\tau)$ is the transition probability matrix in a certain lag time τ and \mathbf{I} are all intermediate states. For the case of the dimer $\mathbf{M} \equiv \{T, D, U\}$, we only define one intermediate state, i.e., $\mathbf{I} = D$, and therefore the committor probability q_D^+ is easily derived,

$$q_D^+ = \frac{T_{DT}}{T_{DT} + T_{DU}}. \quad (20)$$

The overall rate k_{UT}^{TPT} is subsequently given by

$$k_{UT}^{TPT} = \frac{\pi_U (T_{UT} + T_{UD} q_D^+)}{\tau (\pi_U + \pi_D q_D^-)}, \quad (21)$$

where $q_D^- = 1 - q_D^+$, and $\pi_{\mathcal{I}}$ is the population of state \mathcal{I} . The dissociation rate constant k_{TU}^{TPT} can be formulated in a similar fashion.

In addition to the overall (un)binding rate, also the flux between states during association (or dissociation) can be calculated. Here we are mainly interested in the ratio of the flux as follows:

$$\frac{f_{UT}^+}{f_{UDT}^+} = \frac{T_{UT}}{T_{UD} q_D^+}, \quad (22)$$

which gives an insight whether association primarily occurs indirectly via state D or directly from U to T .

G. Simulation details

1. SRTIS

For two-particle dimerization, we consider the three possible (meta)stable states: a bound state T , defined when the patchy interaction $U_{br} < -0.9\epsilon_T$, a decoy intermediate state D defined when the interaction $U_{bd} < -0.9\epsilon_D$, and the unbound state when the particles are separated more than r_c . All interfaces around stable states are defined through the energy of the system. For the bound states T and D , we set interfaces for every $1.5k_B T$ starting from the boundary of the state until the energy is zero. Interfaces for state U are set at low values of energy to guide the system towards state T or D and to be sure whether paths with low energy are properly sampled: $\lambda_U = \{0.0, -10^{-9}, -10^{-3}, -10^{-1}, -0.4, -1.0\}k_B T$.²¹ An example of a converged simulation ($\epsilon_D = 8k_B T$, $\epsilon_{iso} = 0.0$, $\psi = 120^\circ$) showed that $\log g(\lambda_U) = [0, -0.25, -3.2, -5.5, -6.0, -6.3]$, which validates the use of interfaces with very small energy values as the crossing probability decreases quickly for such small values. The interfaces could have been optimized further; however, this would not change the results.

For the constrained tetramer, an additional state I is defined, where only two bonds are formed and the remaining patches are not allowed to form bonds via barrier-less rotation (see Sec. III C). State T is defined when all three bonds are formed, and $U_{tot}^{etr} < -2.7\epsilon_T$. State D is defined when no bonds are formed and the particle is on the opposite side of the complex, and $U_{tot}^{etr} < -2.7\epsilon_{iso}$. The unbound state U is defined when the motile particle is separated more than r_c to any other

particle of the complex. The interfaces of tetramer states are similarly defined as states defined for two particles.

SRTIS simulations were performed with DMC in a cubic periodic box of size 5.7σ . Frames were saved every ten DMC steps. The maximum path length was set to 10^5 frames, to prevent memory overflow (Note that this maximum path length only refers to the transition path times between states, not the dwell times in the states, which might be much longer). A production cycle of 5×10^5 SRTIS cycles was performed after the scale factor for the Wang-Landau biasing was sufficiently low ($<10^{-5}$), where every cycle consisted of 10 shooting, reversal, replica swap and state swap moves. Averages for the crossing probability and path densities were sampled after each move.

2. Potential

For the two-particle system, the attractive strength and the patch angular width of the target site is set to, $\epsilon_T = 15k_B T$ and $\delta = 20^\circ$ degrees, respectively. For the constrained tetramer complex, the attractive strength and the patch angular width of the target sites is set to $\epsilon_T = 5k_B T$ and $\delta = 20^\circ$ degrees, respectively. The potential is truncated at $r_c = 2.0\sigma$.

The strengths of attraction for the dimer were chosen such that the binding affinities are comparable to real proteins, i.e., in the order $\text{nM}^{-1} - \mu\text{M}^{-1}$, corresponding to dissociation rates of order $k_{\text{off}} \approx 10^{-3} - 10^0 \text{ s}^{-1}$. The strength of the tetramer is comparable to the patch strength used in the work of Fusco and Charbonneau.¹² The non-specific isotropic strength was varied up to $\epsilon_{\text{iso}} = 10$, where the association rate reaches a plateau.

III. RESULTS AND DISCUSSION

A. Effect of the decoy binding site on kinetics

1. Rate matrix and population

We first study how an additional decoy binding site affects the overall dimerization rate constant. Consider two particles of diameter σ interacting via an attractive angle-dependent, short-ranged 24-12 Lennard-Jones (LJ) potential with strength $\epsilon_T = 15k_B T$ and a patch-width $\delta = 20^\circ$ (a similar patch-width was used to study proteins^{12,33}). For a protein size $\sigma = 5 \text{ nm}$, this choice corresponds to a dissociation constant of order μM .⁴⁶ In addition, one particle has a decoy binding site placed under an angle ψ away from the target site with the same patch-width and with attractive strength ϵ_D (see Figs. 1 and 2). This system has three meta-stable states: a bound (target) state T , a nonproductive decoy state D , and an unbound state U , which, for the chosen box size of 5.7σ , has the largest equilibrium population.

We perform SRTIS simulations for several values of the decoy strength $\epsilon_D/k_B T = \{2, 4, 6, 8, 10, 12, 14, 16\}$. For each transition, we compute the rate constant via Eq. (15). The resulting rate matrix is plotted in Fig. 3 in units of DMC time steps. The units can be easily translated to real time, depending on the system that the model represents. Using the conversion factors mentioned in Sec. II B, we find that for colloids with a diameter $\sigma = 1 \mu\text{m}$ and a time step of $7 \mu\text{s}$, a rate constant of 10^{-7} corresponds to roughly 0.014 s^{-1} . For proteins, with a

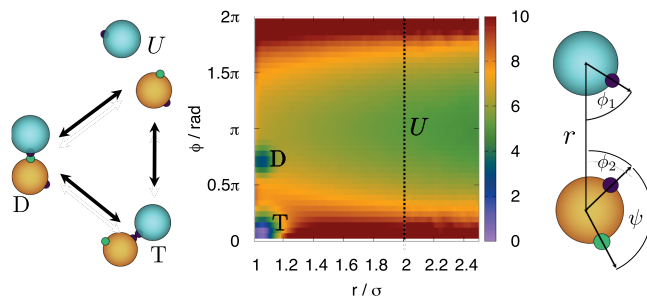


FIG. 2. Left: Association transitions between unbound (U), decoy (D), and target (T) states. Right: Cartoon image of the patchy particle model. The decoy (green) and target (black) sites are separated by angle ψ . The particle distance is $r = |\mathbf{r}_{12}|$, with \mathbf{r}_{12} the center of mass vector. The angles $\phi_i = \arccos(\mathbf{r}_{12} \cdot \mathbf{p}_i / r)$ between the patch vector \mathbf{p}_i and center of mass vector \mathbf{r}_{12} track the orientation. Middle: The free energy landscape obtained from the sampled path ensembles for $\psi = 120^\circ$, $\epsilon_D = 10k_B T$, projected on distance, r , and angle $\phi = \phi_1 + \phi_2$. The bound state T is clearly visible at $r = 1.0\sigma$ and $\phi = 0$. The unbound state U is defined by $r \geq 2.0\sigma$. The decoy state D is visible as a minimum at $\phi = 120^\circ$.

diameter of 10 nm and a DMC time step of around 10^2 ns , a rate constant of 10^{-7} corresponds approximately to 1 s^{-1} .

Rate constants k_{TU} and k_{UT} are nearly independent of ϵ_D , as expected. Only k_{TD} and k_{DT} are dependent on ψ , demonstrating that the rebinding probability from state D to T is significantly larger for $\psi = 60^\circ$. Elements k_{DT} and k_{DU} show expected Arrhenius-like behavior (i.e., an exponential dependence on ϵ) for $\epsilon_D \geq 8k_B T$, whereas at low values of ϵ_D , the rate constant becomes more diffusion influenced as seen from the nonlinear dependence. Note that while the standard usage of ‘‘Arrhenius behavior’’ is to describe the exponential dependence of the rate with the inverse temperature T , we also use it here for the exponential dependence of the rate with the attraction strength ϵ . Since ϵ

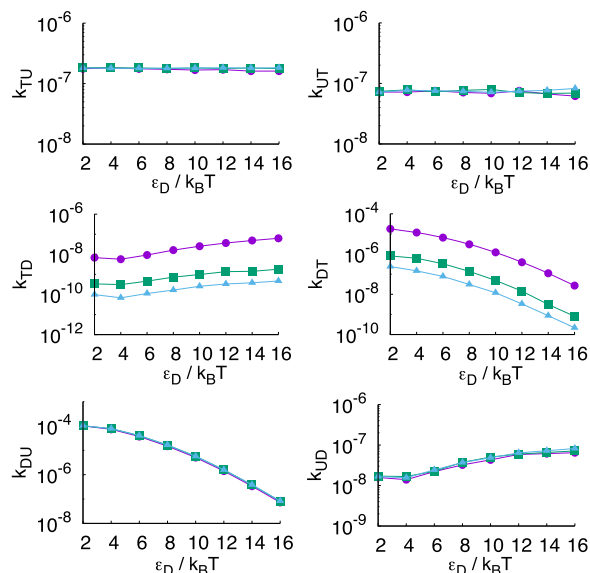


FIG. 3. Rate matrix, \mathbf{K} , for different angles of the decoy patch, $\psi = 60^\circ$ (circles), $\psi = 120^\circ$ (squares), and $\psi = 180^\circ$ (triangles). Rate constants k_{TU} and k_{UT} are hardly dependent on ϵ_D as expected. Moreover, only k_{TD} and k_{DT} are dependent on ψ . Elements k_{DT} and k_{DU} show expected Arrhenius-like behaviour after $\epsilon_D \approx 8k_B T$. However, at low values of ϵ_D , diffusion limits become more dominant. All rates are reported in units of DMC time steps.

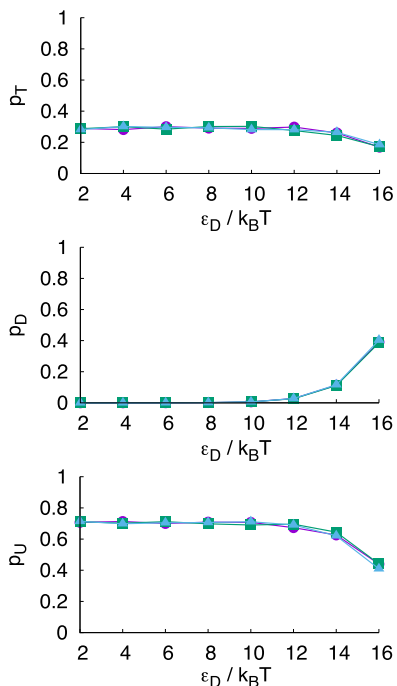


FIG. 4. Equilibrium population of T , D , and U as a function of the decoy interaction strength for different values of $\psi = 60^\circ$ (circles), 120° (squares), and 180° (triangles). Clearly, the decoy state only becomes higher populated when $\epsilon_D > \epsilon_T$. Moreover, due to the box size, the population of U is always higher. Also note that the populations are not dependent on ψ .

always appears in combination with $1/k_B T$, this identification is natural.

From the rate matrix, we can obtain the equilibrium population by computing the zeroth eigenvector or alternatively apply the long time limit of $p(t) = \exp(\mathbf{K}t)$. These populations are shown in Fig. 4. The decoy state only has a larger population than the bound state when $\epsilon_D > \epsilon_T$. Moreover, due to the size of the box, the population of U is always the highest of the three states. While the populations shift toward D with increasing ϵ_D , they are independent of ψ , indicating that the effect of rebinding is only affecting the kinetics of the system, not the thermodynamic equilibrium, as expected [see also the free energy landscape projection of the path ensembles in Fig. 2(b)].

2. Effective rate constants

We extract the overall rate constants, k_{UT}^{TPT} and k_{TU}^{TPT} , from the rate matrix, using Transition Path Theory (TPT)⁴⁵ via Eq. (21), shown as a function of ϵ_D in Fig. 5.

As expected, the overall association rate constant $k_{on} \equiv k_{UT}^{TPT}$ does not change much for low ϵ_D but decreases for high $\epsilon_D > 12k_B T$, as pathways that reach D will not significantly contribute to association. Also, the dissociation rate constant $k_{off} \equiv k_{TU}^{TPT}$ drops only minimally at high $\epsilon_D = 16k_B T$. The transition from D to T is less likely than that from D to U within these conditions, as the patch alignment requirement limits the possible kinetic pathways to state T .

One could argue that there is no increase in the association rate constant due to the fact that the volume of the box is small. Usual protein concentrations are much lower (*e.g.*, nM – μ M) than what is simulated here ($\sim \mu$ M) when σ is taken as

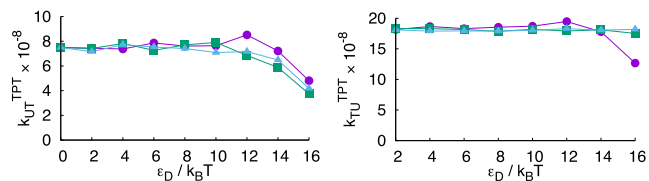


FIG. 5. Overall association (left) and dissociation (right) rate constants calculated via TPT as a function of ϵ_D for different values of $\psi = 60^\circ$ (circles), 120° (squares), and 180° (triangles). Even though the reactive path density in Fig. 6 shows probability from D to T , the decoy state has little effect on the overall association or dissociation irrespective of the position relative to the target site, due to $k_{DU} > k_{DT}$ for each ϵ_D . At high ϵ_D , the decoy site has a negative effect on the association rate constant which halves at high ϵ_D almost independent of ψ .

5 – 10 nm, a typical protein size. Naively, one would assume that with larger volume the presence of an additional binding site which keeps the particles in close proximity should increase the rate constant relatively to no additional binding site, due to rebinding. However, k_{DU} is always significantly larger than k_{DT} (see Fig. 3) which shows that when the volume is enlarged, the non-specific site will still not contribute to the association rate constant as the system will more likely go back to the unbound state than progress towards the bound state. It is interesting that the process from D to T is apparently more unlikely than that from D to U within these conditions, which is a manifestation of the fact that the requirement of precise alignment to bind due to the patchiness of particles limits the kinetic pathways possible for systems to reach their most stable state. Of course, when the decoy binding site moves even closer to the target state, this will change due to lowering of the D - T barrier.

3. Free energy and reaction path density

In the first row of Fig. 6, we show the free energy landscape for three different values of ψ obtained via Eq. (17) with the distance between the centers of the two particles, r , and the angle $\phi = \phi_1 + \phi_2$, where $\phi_i = \arccos(\mathbf{r}_{12} \cdot \mathbf{p}_i/r)$, as the

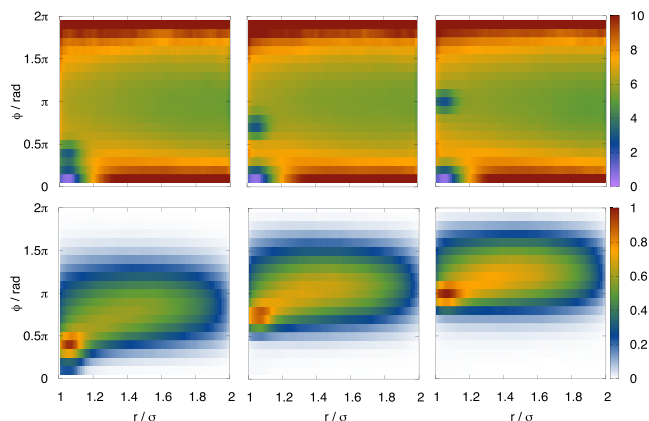


FIG. 6. First row: Free energy landscape for distance between the centers, r , and the sum of the angles of patch vectors with the inter-particle vector, ϕ for $\epsilon_D = 12k_B T$ and from left to right $\psi = 60^\circ$, 120° , and 180° . The free energy is shifted such that the minimum value (T state) is zero. All minima due to the stable states are visible where it is clear where the D state is located as ψ is changed. Second row: Corresponding reactive path density (RPD) for state D . There is only a significant probability from D to T for $\psi = 60^\circ$. However, the transition from D to U dominates the reactive transitions out of state D . Note that integration of a reactive path distribution does not result in unity.

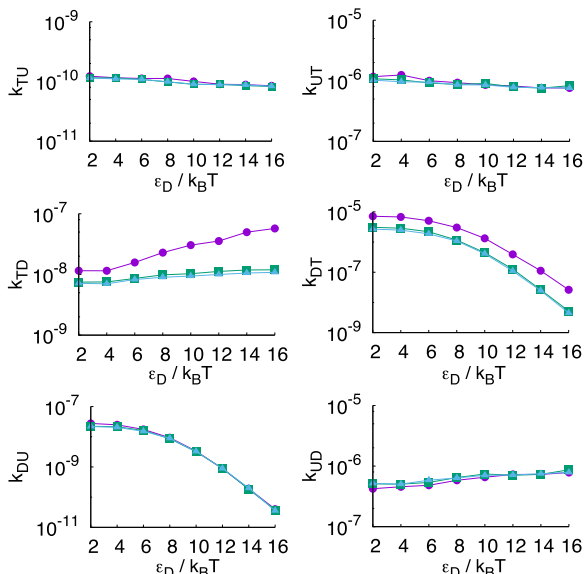


FIG. 7. Rate matrix, \mathbf{K} , for different angles of the decoy patch, $\psi = 60^\circ$ (circles), $\psi = 120^\circ$ (squares), and $\psi = 180^\circ$ (triangles) with a non-specific isotropic interaction of $\epsilon_{iso} = 10k_B T$. Rate constants k_{TU} and k_{UT} are not dependent on ϵ_D and there is no dependency on ψ for k_{DU} as expected. For the rebinding rate constants k_{DT} and k_{TD} , there is no difference between $\psi = 120^\circ$ or 180° , only for $\psi = 60^\circ$.

collective variables that capture the translational and rotational degrees of freedom during the (un)binding process between all three states (see also Fig. 2). The bound state T is clearly visible at $r = 1.0\sigma$ and $\phi = 0$. (Note that the ϕ_i variable is identical to the θ_i variable used in the potential energy. We still use two different variable names, to emphasize that these variables do not have to be the same in general, since we are free to choose any collective variable.)

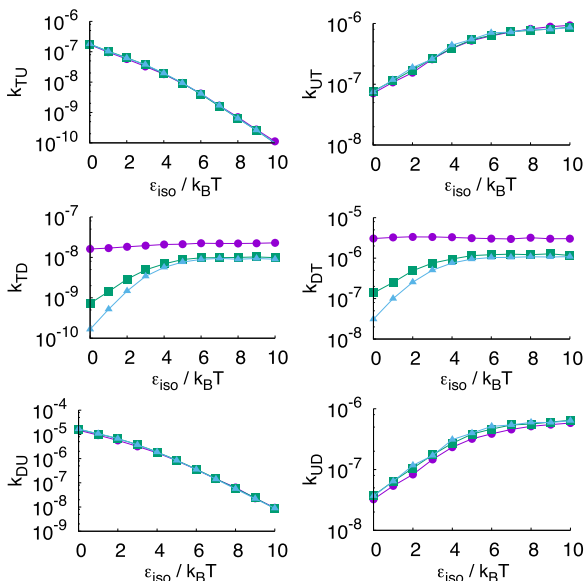


FIG. 8. Rate matrix, \mathbf{K} , for different angles of the decoy patch, $\psi = 60^\circ$ (circles), $\psi = 120^\circ$ (squares), and $\psi = 180^\circ$ (triangles) with a decoy interaction of $\epsilon_D = 8k_B T$. Naturally, k_{TU} and k_{DU} show Arrhenius-like behavior for strong ϵ_{iso} . There is no dependency on ψ for k_{TU} , k_{UT} , and k_{DU} as expected. Interestingly, for $\psi = 120^\circ$ and 180° , k_{DT} and k_{TD} level off around $\epsilon_{iso}/k_B T = 4$, whereas for $\psi = 60^\circ$, there is no dependency at all on ϵ_{iso} .

The unbound state is located beyond the line given by $r = 2.0\sigma$ (see Fig. 2). The intermediate state D is located at different values of ϕ corresponding to $\psi = 60^\circ$, 120° , or 180° . Mechanistic information can be obtained from the path ensemble by plotting the reactive path density (RPD). In Fig. 6, the RPD is plotted for state D defined by Eq. (18). The RPD demonstrates that a transition from T to D instead of U is very improbable (has a low density) when ψ is large, as most probably paths end up in U (located at $r = 2.0\sigma$), which corroborates with the low values of k_{DT} . Only for small ψ is there a significant probability to transition from D to T .

B. Effect of isotropic non-specific interaction

1. Rate matrices

Next, we add a non-specific isotropic interaction between the two particles of the dimer and conduct SRTIS simulations for a range of values $\epsilon_{iso}/k_B T = 0, 1, 2, 3, 4, 5, 6, 7, 8, 9, 10$, each for different values of ϵ_D .

In Fig. 7, the elements of the rate matrices are shown as a function of ϵ_D for $\epsilon_{iso} = 10k_B T$, while in Figs. 8 and 9, the rate matrix elements are plotted as a function of ϵ_{iso} for $\epsilon_D = 8k_B T$ and $\epsilon_D = 16k_B T$, respectively.

Comparing Figs. 3 and 7, an isotropic interaction $\epsilon_{iso} = 10k_B T$ increases the binding rate constants k_{UT} and k_{UD} by an order of magnitude relative to the rate constants without the isotropic attraction. Furthermore, Fig. 7 shows no difference in the rebinding rate constant k_{TD} for $\psi = 120^\circ$ and 180° , whereas when $\psi = 60^\circ$, k_{TD} increases more sharply.

The rate matrices in Figs. 8 and 9 show that k_{TU} and k_{DU} behave Arrhenius-like for strong ϵ_{iso} or ϵ_D . For small ϵ_D , the kinetics becomes dominated by ϵ_{iso} , and vice versa. Interestingly, both k_{DT} and k_{TD} reach a plateau for $\epsilon_{iso}/k_B T > 4$, where rebinding dominates over escape. Moreover, for $\psi = 60^\circ$, k_{DT}

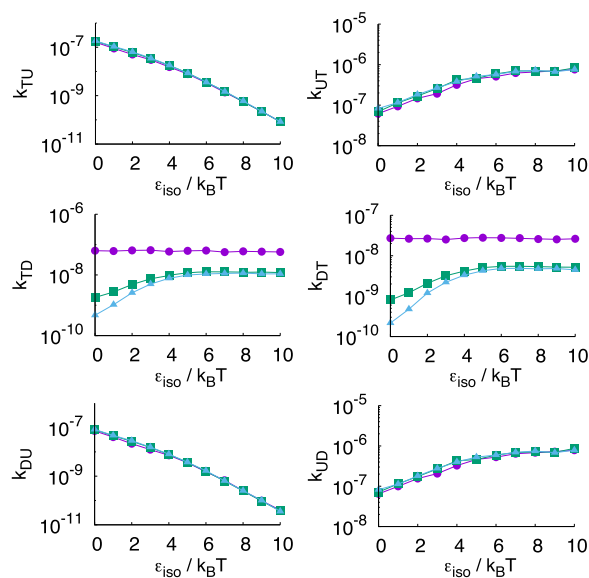


FIG. 9. Rate matrix, \mathbf{K} , for different angles of the decoy patch, $\psi = 60^\circ$ (circles), $\psi = 120^\circ$ (squares), and $\psi = 180^\circ$ (triangles) with a decoy interaction of $\epsilon_D = 16k_B T$. Similar trends are visible as in Fig. 8, except for k_{DU} and k_{DT} which are significantly lower.

and k_{TD} are relatively high and hardly change with ϵ_{iso} , indicating that the chance of rebinding is high for small ψ , due to a (partial) overlap of the patches, lowering the barrier for the D to T transition. For larger ψ angles, increasing the ϵ_{iso} isotropic interaction leads to an enhanced rebinding probability. Note that changing ϵ_D only really alters the exit rate constants from decoy state D (see also Fig. 7).

2. Path density

Figure 10 gives mechanistic information of the rebinding effect in the form of the reactive path density (RPD) for transitions out of D , obtained from the path ensembles. The rebinding probability increases between $\epsilon_{iso} = 2k_B T$ and $\epsilon_{iso} = 6k_B T$ and saturates for high $\epsilon_{iso} = 12k_B T$. While a transition from D to T instead of U is probable (has a high density) for small ψ or high ϵ_{iso} , it is very improbable for large ψ and small ϵ_{iso} , as most paths end up in U ($r \geq 2.0\sigma$).

3. Effective rate constants

Figure 11 shows the effect of both non-specific isotropic interaction ϵ_{iso} and decoy interaction ϵ_D on the overall association rate constant, k_{UT}^{TPT} , computed using Eq. (21). Clearly, k_{UT}^{TPT} increases by more than an order of magnitude with the isotropic interaction ϵ_{iso} for low decoy interaction ϵ_D but eventually levels off at high attraction, i.e., $\epsilon_{iso} \gtrsim 8$. However, adding the isotropic interaction does not affect the association rate constant for high decoy interaction $\epsilon_D = 16$. As the decoy patch becomes more attractive, the increase in k_{on} gained due to the non-specific interaction is lost. In this region, it is just as probable to end up in D as in T , since both the target and decoy sites are of equal strength. This consequently retards the overall association toward the target state. The effect of the decoy strength is clearly to lower k_{UT}^{TPT} , for each setting of the ϵ_{iso} . Note that the opposing effect of the decoy site is much stronger when there is non-specific isotropic interaction. This is at first sight surprising but is a direct consequence of the shift in equilibrium population due to the isotropic interaction,

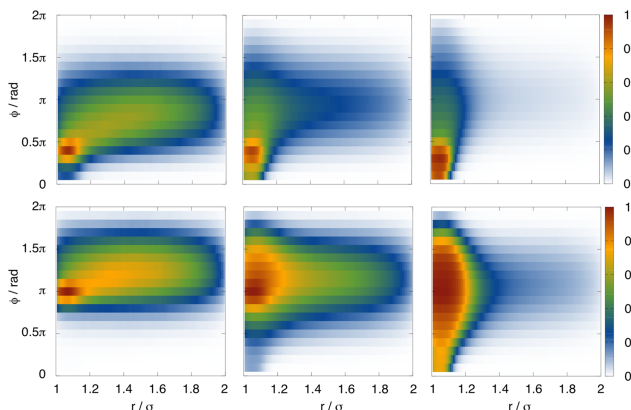


FIG. 10. Effect of isotropic interaction on the reactive path density (RPD) for state D with $\epsilon_D = 12k_B T$ as a function of the distance r and the angle ϕ , for $\psi = 60^\circ$ (top row) and $\psi = 180^\circ$ (bottom row), from left to right for $\epsilon_{iso} = 2, 6, 12k_B T$. The transition from D to U dominates the paths out of state D for low $\epsilon_{iso} \leq 6$. There is only a significant rebinding probability from D to T for $\psi = 60^\circ$ or for high ϵ_{iso} .

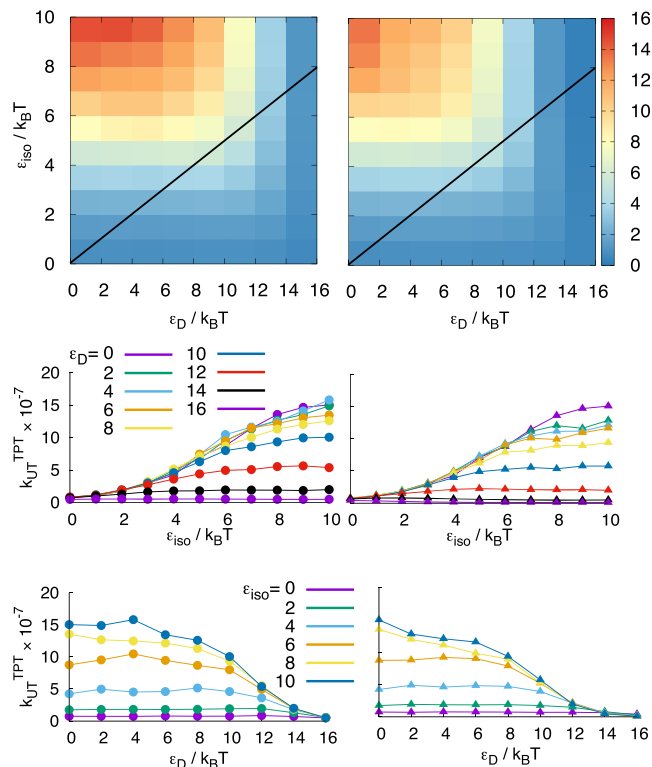


FIG. 11. Top row: Heat map of the overall association rate $10^7 \times k_{UT}^{TPT}(\psi, \epsilon_{iso}, \epsilon_D)$ for $\psi = 60^\circ$ (left) and 180° (right). The diagonal lines indicate the effect of cooperativity in the tetramer on the overall rate constants. For low ψ , a higher maximum overall association rate constant is reached along the diagonal. Lower panels: Different cuts through the parameter space for the overall association rate. Middle row: $k_{UT}^{TPT}(\psi, \epsilon_{iso}, \epsilon_D)$ for different decoy strengths, as a function of ϵ_{iso} . Bottom row: $k_{UT}^{TPT}(\psi, \epsilon_{iso}, \epsilon_D)$ for different isotropic strengths, as a function of ϵ_D . All rates are in units of DMC time steps. The rate constants increase with non-specific isotropic interaction but decrease for high ϵ_D values.

making effectively the $D - T$ transition the relevant barrier to overcome [as is also clear from Eq. (21)].

Non-specific isotropic interactions of more than a few $k_B T$ will lead to condensation. The short-ranged 24-12 LJ potential used here leads to a metastable vapor-liquid coexistence line with respect to the fluid-solid line.³⁰ For high ϵ_{iso} , crystallization can only be avoided at very low concentration. Our results are robust against lowering the concentration (see Fig. 15 of the [supplementary material](#)). Furthermore, by using a shorter ranged potential, *e.g.*, a 100-50 LJ potential, the fluid-solid line will shift significantly, whereas the effect of the non-specific isotropic interaction on the association kinetics will not change qualitatively.

4. Preferred mechanism

We infer the preferred association mechanism from the TPT fluxes. Figure 12 plots the net flux ratio f_{UT}/f_{UDT} computed via Eq. (22), for a strong decoy $\epsilon_D = 14$. The higher rebinding probability for a low ψ results in more associating pathways via D than for high ψ , *i.e.*, a lower flux ratio f_{UT}/f_{UDT} . Thus, direct paths are dominant for low ϵ_{iso} and for high ψ , as rebinding is very rare for these settings. The flux ratio never drops below unity, even when all paths exiting D rebound correctly to T , since the chances of going to the D or T state from the unbound state U are about equal.

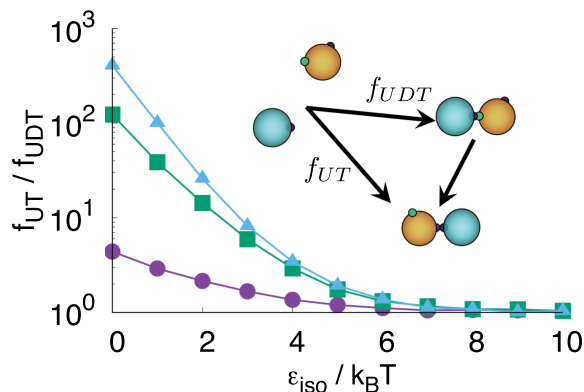


FIG. 12. Flux ratio f_{UT}/f_{UDT} as a function of ϵ_{iso} for a decoy site with $\epsilon_D = 14k_B T$ and $\psi = 60^\circ$ (circles), $\psi = 120^\circ$ (squares), and $\psi = 180^\circ$ (triangles). Higher rebinding probability for $\psi = 60^\circ$ results in lower f_{UT}/f_{UDT} indicating more reactive pathways from U to T via D compared to higher values of ψ .

C. Constrained tetrahedron formation

Protein complexes frequently consist of more than two proteins. We study the formation kinetics of a model tetramer complex in which each protein has three binding sites. The rate determining step in the tetramer formation is the addition of a single protein to a correctly formed trimer. In previous work, we studied the influence of rotational diffusion²¹ and of the multivalency⁴⁷ on the formation kinetics of this “constrained tetrahedron.”²¹ Here, we investigate the effect of adding an isotropic non-specific interaction to each protein. We use the same interaction non-specific potential between particles as for the dimer; only now the particles have three patches put at the contact points of a perfect tetrahedral arrangement of the particles (see Sec. II A). In this patchy particle system, there are four stable states, U , T , I , and D (see Fig. 13 for a schematic representation). Starting in the unbound state U (one particle far

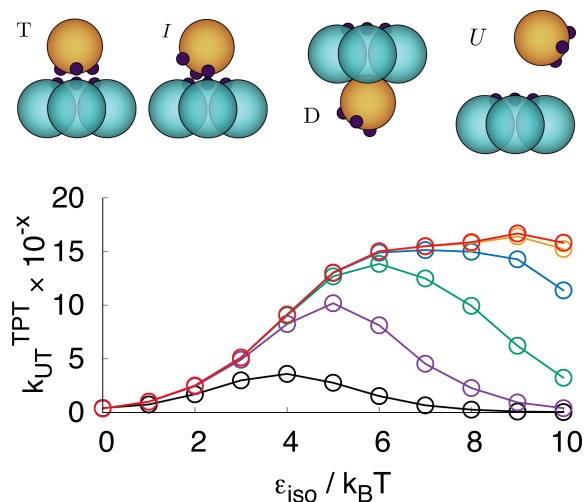


FIG. 13. Top: Cartoon images of states defined for the constrained tetrahedron system with the motile particle in orange. Bottom: Overall association rate constant k_{UT}^{TPT} as a function of ϵ_{iso} for different concentrations by scaling the volume with V/V_0 , where V_0 is the simulation volume. The rate constants are scaled with a factor 10^x to fit in the same plot, where $V/V_0 = 1.0$ (black, $x = 7$), 10.0 (purple, $x = 8$), 10^2 (green, $x = 9$), 10^3 (blue, $x = 10$), 10^4 (orange, $x = 11$), and 10^5 (red, $x = 11$). The maximum in the association rate constant shifts from $4k_B T$ to $8k_B T$ for decreasing concentration.

away from the correctly formed trimer), the incoming particle can bind to the fixed trimer correctly by forging all three bonds (the T state) or could be trapped in an intermediate state where two frustrated patchy bonds are formed. Note that for this system a patch interaction $\epsilon_T = 5k_B T$ yields the same total energy for state T as for the dimer. The additional non-specific isotropic potential results in a fourth (meta)stable state, D , where the incoming particle is trapped on the opposite side of the trimer, forming no specific patchy bonds, but only interacting via isotropic potentials. In this state, the attaching protein interacts with the three particles of the fixed trimer simultaneously. Therefore rearrangement into the productive state can only occur by losing at least one non-specific isotropic interaction. As the trimer can be seen as a rigid body with a (trivalent) target binding site and the D state as a decoy state, at first sight this situation seems very similar or (almost) identical to the binding of two particles with a decoy state, as discussed above. To investigate the similarity/difference between the two cases, we compute the 4×4 association rate matrix with SRTIS, for several values of the attractive isotropic interaction, ϵ_{iso} (see Fig. 6 of the [supplementary material](#)). In Fig. 13, we plot the overall association rate constant as a function of ϵ_{iso} . Strikingly, the rate constant increases first and then decreases with non-specific isotropic interaction. Remarkably, the increase is relatively strongest for the lowest concentration. The maximum in the association rate constant shifts for decreasing concentration from $4k_B T$ to $8k_B T$. The behavior of the overall dissociation rate constant roughly follows Arrhenius-like behavior (see Fig. 8 of the [supplementary material](#)).

One might think that the case of the constrained tetrahedron would be almost identical to the non-specific decoy case with only a slightly different geometry. However, the behavior is qualitatively different due to the cooperativity of the non-specific interaction in the trimer. This unexpected difference between the tetramer and the dimer systems can be reconciled by realizing that for the tetramer, the decoy state potential is not fixed but changes with ϵ_{iso} as $U_D = 3\epsilon_{iso}$, ignoring the configurations in which the attaching protein is bound to two particles. This corresponds to a dimer with $U_D = \epsilon_{iso} + \epsilon_D$ so that the two systems behave similarly for approximately $\epsilon_D = 2\epsilon_{iso}$. This relation specifies a diagonal cut through the parameter space $\epsilon_{iso}, \epsilon_D$ plotted in the 2D heat map representation in Fig. 11. Indeed, the maximum in the association rate along this diagonal qualitatively explains the behavior of the tetramer formation. These results indicate that rebinding effects due to the isotropic potential enhance association for dimer systems but can suppress it for larger complexes.

IV. CONCLUSIONS

In this work, we have investigated the effect of the presence of additional binding sites as well as nonspecific isotropic interaction on the association kinetics of patchy particle colloid and protein models. In general, we find that additional anisotropic potentials suppress overall association kinetics, while adding an isotropic potential enhances it. This can be understood in energy landscape terms. An isotropic potential corresponds to a smooth energy landscape that is easy to navigate for the dimer. A rougher energy landscape, such

as induced by (deep) potential minima, causes kinetic trapping, hampering the search for global minima. Surprisingly, the enhancement that is gained by the isotropic potential completely vanishes for kinetic traps of more than $8 k_B T$. Our prediction is thus that natural protein or colloid association kinetics can accommodate binding traps up to a certain strength but not much higher. This threshold will depend on potential shape; a narrower anisotropic potential than the 20° angle used here will raise the threshold; a broader one will lower it. Our results suggest that if optimal association kinetics is important, e.g., for signaling or cellular response, evolution should tend to smooth the energy landscape for binding, although a certain amount of roughness can be sustained. If such optimal binding kinetics is selected for, one would even expect an energy landscape with a gradient toward the binding site.

In addition, the association kinetics of complexes becomes shape dependent. For the formation of a tetramer, we found non-monotonic association rate constants as a function of the nonspecific isotropic interaction, caused by an induced decoy site. This suggests that for successful complex formation, a non-specific isotropic interaction has to be limited in strength, as cooperativity can oppose the enhancement in association kinetics. These insights can also be used as a design principle for enhancing soft matter self-assembly by dressing patchy particles with a smooth non-specific isotropic attraction and ensuring that nonproductive patchy interactions are not too strong.⁴⁸ Experimentally, the isotropic potential can be altered via ionic strength, pH, depletant, or temperature,¹⁴ while specific interaction can be designed, e.g., by sequence mutation.

Our methodology can be applied with arbitrary protein or colloid potentials. In more complex systems, such as realistic, large proteins, a challenge will be to construct a reasonable order parameter describing the interfaces around the states. In this work, we used the energy of the pair interaction, and something similar might be appropriate for a more complex system as well. In general, the problem of the choice of the order parameter is not solved, although the transition interface sampling methods are much more forgiving in that respect than other rare event methods,⁴⁹ save for straightforward dynamics.

Finally, the applied methodology allows evaluation of rate matrices up to moderate complexity (up to tens of states). This is important for the multiscale modeling of biochemical networks^{50,51} and biomolecular or soft-matter self-assembly.¹⁸

SUPPLEMENTARY MATERIAL

See [supplementary material](#) for additional information on the effective rate constants, path length distributions, and reactive path densities for the dimer, as well as rate constant matrices and effective rate constants for the tetramer system.

ACKNOWLEDGMENTS

This work is part of the research programme of the Foundation for Fundamental Research on Matter (FOM), which is part of the Netherlands Organization for Scientific Research (NWO). D.W.H.S. acknowledges support from the E-CAM Center of Excellence, which received funding from

the European Union's Horizon 2020 research and innovation programme under Grant Agreement No. 676531.

- ¹V. Dahirel, F. Paillusson, M. Jardat, M. Barbi, and J.-M. Victor, *Phys. Rev. Lett.* **102**, 228101 (2009).
- ²O. G. Berg and P. H. von Hippel, *Annu. Rev. Biophys. Biophys. Chem.* **14**, 131 (1985).
- ³S. H. Northrup and H. P. Erickson, *Proc. Natl. Acad. Sci. U. S. A.* **89**, 3338 (1992).
- ⁴S. E. Halford and J. F. Marko, *Nucleic Acids Res.* **32**, 3040 (2004).
- ⁵R. R. Gabdouliline and R. C. Wade, *J. Mol. Recognit.* **12**, 226 (1999).
- ⁶G. Schreiber, G. Haran, and H.-X. Zhou, *Chem. Rev.* **109**, 839 (2009).
- ⁷G. Schreiber, *Curr. Opin. Struct. Biol.* **12**, 41 (2002).
- ⁸K. Takahashi, S. Tănase-Nicola, and P. R. Ten Wolde, *Proc. Natl. Acad. Sci. U. S. A.* **107**, 2473 (2010).
- ⁹A. Vijaykumar, P. G. Bolhuis, and P. R. ten Wolde, *Faraday Discuss.* **195**, 421 (2016).
- ¹⁰N. Agmon and A. Szabo, *J. Chem. Phys.* **92**, 5270 (1990).
- ¹¹E. Bianchi, R. Blaak, and C. N. Likos, *Phys. Chem. Chem. Phys.* **13**, 6397 (2011).
- ¹²D. Fusco and P. Charbonneau, *Phys. Rev. E* **88**, 012721 (2013).
- ¹³I. V. Gopich and A. Szabo, *Proc. Natl. Acad. Sci. U. S. A.* **110**, 19784 (2013).
- ¹⁴J. N. Israelachvili, *Intermolecular and Surface Forces*, 3rd ed. (Academic Press, 2011).
- ¹⁵Y. Wang, Y. Wang, D. R. Breed, V. N. Manoharan, L. Feng, A. D. Hollingsworth, M. Weck, and D. J. Pine, *Nature* **491**, 51 (2012).
- ¹⁶D. J. Kraft, R. Ni, F. Smalenburg, M. Hermes, K. Yoon, D. A. Weitz, A. van Blaaderen, J. Groenewold, M. Dijkstra, and W. K. Kegel, *Proc. Natl. Acad. Sci. U. S. A.* **109**, 10787 (2012).
- ¹⁷L. Colón-Meléndez, D. J. Beltran-Villegas, G. van Anders, J. Liu, M. Spellings, S. Sacanna, D. J. Pine, S. C. Glotzer, R. G. Larson, and M. J. Solomon, *J. Chem. Phys.* **142**, 174909 (2015).
- ¹⁸A. C. Newton, T. A. Nguyen, S. J. Veen, D. J. Kraft, P. Schall, and P. G. Bolhuis, *Soft Matter* **13**, 4903 (2017).
- ¹⁹T. A. Nguyen, A. Newton, S. J. Veen, D. J. Kraft, P. G. Bolhuis, and P. Schall, *Adv. Mater.* **29**, 1700819 (2017).
- ²⁰E. Jankowski and S. C. Glotzer, *Soft Matter* **8**, 2852 (2012).
- ²¹A. C. Newton, J. Groenewold, W. K. Kegel, and P. G. Bolhuis, *Proc. Natl. Acad. Sci. U. S. A.* **112**, 15308 (2015).
- ²²C. Gögelein, G. Nägele, R. Tuinier, T. Gibaud, A. Stradner, and P. Schurtenberger, *J. Chem. Phys.* **129**, 085102 (2008).
- ²³A. W. Wilber, J. P. K. Doye, A. A. Louis, and A. C. F. Lewis, *J. Chem. Phys.* **131**, 175102 (2009).
- ²⁴M. G. Noro and D. Frenkel, *J. Chem. Phys.* **113**, 2941 (2000).
- ²⁵G. Foffi and F. Sciortino, *J. Phys. Chem. B* **111**, 9702 (2007).
- ²⁶G. Odriozola and M. Lozada-Cassou, *Phys. Rev. Lett.* **110**, 105701 (2013).
- ²⁷F. Romano, C. De Michele, D. Marenduzzo, and E. Sanz, *J. Chem. Phys.* **135**, 124106 (2011).
- ²⁸W.-N. Du and P. G. Bolhuis, *J. Chem. Phys.* **139**, 044105 (2013).
- ²⁹W. Du and P. G. Bolhuis, *J. Chem. Phys.* **140**, 195102 (2014).
- ³⁰M. Nayhouse, V. R. Heng, A. M. Amlani, and G. Orkoulas, *J. Phys.: Condens. Matter* **24**, 375105 (2012).
- ³¹D. Chandler and J. D. Weeks, *Phys. Rev. Lett.* **25**, 149 (1970).
- ³²J. D. Weeks, D. Chandler, and H. C. Andersen, *J. Chem. Phys.* **54**, 5237 (1971).
- ³³H. Liu, S. K. Kumar, and F. Sciortino, *J. Chem. Phys.* **127**, 084902 (2007).
- ³⁴A. J. Williamson, A. W. Wilber, J. P. Doye, and A. A. Louis, *Soft Matter* **7**, 3423 (2011).
- ³⁵C. Dellago, P. Bolhuis, and P. L. Geissler, *Adv. Chem. Phys.* **123**, 1 (2002).
- ³⁶P. G. Bolhuis, *J. Chem. Phys.* **129**, 114108 (2008).
- ³⁷T. S. van Erp, D. Moroni, and P. G. Bolhuis, *J. Chem. Phys.* **118**, 7762 (2003).
- ³⁸T. S. van Erp, *Phys. Rev. Lett.* **98**, 268301 (2007).
- ³⁹P. G. Bolhuis and W. Lechner, *J. Stat. Phys.* **145**, 841 (2011).
- ⁴⁰J. Rogal and P. G. Bolhuis, *J. Chem. Phys.* **129**, 224107 (2008).
- ⁴¹A. M. Ferrenberg and R. H. Swendsen, *Phys. Rev. Lett.* **63**, 1195 (1989).
- ⁴²S. Kumar, D. Bouzida, R. H. Swendsen, P. A. Kollman, and J. M. Rosenberg, *J. Comput. Chem.* **13**, 1011 (1992).
- ⁴³P. G. de Gennes, *J. Chem. Phys.* **76**, 3316 (1982).
- ⁴⁴J. Rogal, W. Lechner, J. Juraszek, B. Ensing, and P. G. Bolhuis, *J. Chem. Phys.* **133**, 174109 (2010).

- ⁴⁵F. Noé, C. Schütte, E. Vanden-Eijnden, L. Reich, and T. R. Weikl, *Proc. Natl. Acad. Sci. U. S. A.* **106**, 19011 (2009).
- ⁴⁶When including the isotropic nonspecific interaction, the dissociation constant lowers to order nM.
- ⁴⁷A. C. Newton, J. Groenewold, W. K. Kegel, and P. G. Bolhuis, *J. Chem. Phys.* **146**, 234901 (2017).
- ⁴⁸S. Whitlam and R. L. Jack, *Annu. Rev. Phys. Chem.* **66**, 143 (2015).
- ⁴⁹T. S. van Erp, *J. Chem. Phys.* **125**, 174106 (2006).
- ⁵⁰A. Vijaykumar, P. G. Bolhuis, and P. R. ten Wolde, *J. Chem. Phys.* **143**, 214102 (2015).
- ⁵¹A. Vijaykumar, T. E. Ouldridge, P. R. ten Wolde, and P. G. Bolhuis, *J. Chem. Phys.* **146**, 114106 (2017).